Science
AAAS

Supplementary Material for:

Mass-Resolved Electronic Circular Dichroism Ion Spectroscopy

Steven Daly,[1] Frédéric Rosu,[2] Valérie Gabelica[1]*

[1]Université de Bordeaux, Inserm & CNRS, Laboratoire Acides Nucléiques: Régulations Naturelle et Artificielle (ARNA, U1212, UMR5320), IECB, 2 rue Robert Escarpit, 33607 Pessac, France.

[2] Université de Bordeaux, CNRS & Inserm, Institut Européen de Chimie et Biologie (IECB, UMS3033, US001), 2 rue Robert Escarpit, 33607 Pessac, France.

*Correspondence to: v.gabelica@iecb.u-bordeaux.fr.

This file includes:

Materials and Methods

Sample preparation

All DNA strands with D-sugars were purchased from Eurogentec (Liège, Belgium) with RP-cartridge purification and used as received. The L-dTGGGGT strand was purchased from Biomers Gmbh (Ulm, Germany) with HPLC purification and used as received. Nuclease-free water was from Ambion (Fischer Scientific, Illkirch, France). Ammonium acetate (NH_4OAc, BioUltra ~ 5M, Fluka), trimethylammonium acetate (TMAA, Ultra for UPLC ~ 1M, Fluka), and potassium (KCl, > 99.999%, Sigma) were purchased from Sigma-Aldrich (Saint-Quentin Fallavier, France).

The single strand dTGGGGT was dissolved in nuclease free H_2O to a concentration of 800 µM. This was diluted to 200 µM in 150 mM aqueous NH_4OAc and left overnight at 4 °C to yield a 50 µM quadruplex stock solution. This forms the $[(dTGGGGT)_4 \bullet (NH_4^+)_3]$ tetramolecular G-quadruplex, abbreviated **TG4T** (average mass of 5- complex: 7499.1 Da). For use in the ESI source, the stock solution was diluted to 5 µM G-quadruplex in 100 mM aqueous NH_4OAc.

The single strand $d(T(GGT)_4TG(TGG)_3TGTT)$ was dissolved in nuclease free H_2O to a concentration of 200 µM. This solution was diluted to 50 µM in 150 mM aqueous NH_4OAc and left overnight at 4 °C to yield a stock solution. This forms the $[dT(GGT)_4TG(TGG)_3TGTT \bullet (NH_4^+)_3]$ intramolecular G-quadruplex, abbreviated **ZG4** (average mass of 5- complex: 8901.8 Da). For use in the ESI source, the stock solution was diluted to 5 µM in 150 mM NH_4OAc.

The single strand dG_{11} was dissolved in nuclease free H_2O to a concentration of 200 µM. $AgNO_3$ was prepared in H_2O at 1 mM. A stock solution with 50 µM dG_{11} and 650 µM $AgNO_3$ was prepared in 10 mM NH_4OAc, giving a small excess of Ag^+ compared to the number of guanine base pairs. The stock solution was left at room temperature overnight to allow the formation of the duplex ($[(dG_{11})_2 \bullet (Ag^+)_{11}]$, abbreviated **GAgG** (average mass of 5- complex: 8289.2 Da). For use in the ESI source, the stock solution was diluted to 5 µM duplex in 10 mM NH_4OAc.

The single strand d(GGGTTAGGGTTAGGGTTTGGG) was dissolved in nuclease free H_2O to a concentration of 200 µM. A stock solution of 50 µM strand in 1 mM KCl 100 mM trimethylammonium acetate (TMAA) was annealed at 80°C for 5 minutes and left overnight at room temperature to fold into a quadruplex. This forms the $[d(GGGTTA)_2GGGTTTGGG \bullet (K^+)_2]$ intramolecular G-quadruplex, abbreviated **5YEY** (average mass of 5- complex: 6715.5 Da). For use in the ESI source, the quadruplex was diluted to 5 µM in 1 mM KCl and 100 mM TMAA.

The single strand d(TAGGGTTAGGGTTAGGGTTAGGG) (abbreviated **23TAG**) was dissolved in nuclease free H_2O to a concentration of 200 µM. A stock solution of 5 µM strand in 0.4 mM KCl and 100 mM trimethylammonium acetate (TMAA) was annealed at 85°C for 5 minutes, then left overnight at 4°C to fold the mixture of 1-K^+ and 2-K^+ quadruplexes (average mass of 5- complex with 1K: 7303.9 Da; with 2K: 7341.0 Da) (*33*).

Gas phase experimental setup

The experimental setup used for all gas phase experiments is shown in Fig. S4. The light source is a Spectra Physics PRO-230-30 Nd:YAG laser (355 nm) pumping a GWU Premiscan OPO running at 30 Hz, producing UV photons between 295 and 230 nm for our experiments. The laser is guided through a telescope, using an achromatic doublet (f = 200 mm) and a fused silica lens (f = -100 mm). The lenses are separated by 130 mm to obtain a collinear beam. Neutral density filters (0 to 0.5 optical density, combined range between 0 and 1.0) are fitted in two separate wheel mounts before and after the telescope, allowing to control the pulse energy. The beam then passes through an electro-mechanical shutter (SRS 470), which controls the number of pulses used to irradiate the ions. The shutter is synchronized to the laser and mass spectrometer cycle to ensure irradiation with a single pulse during the MS/MS activation stage of the mass spectrometer.
Next, the laser is guided through cage-mounted polarization optics. Firstly, a thin fused silica blade is used to reflect a portion of the beam to a pyroelectric energy meter (Ophir PE9-C), which can be used to constantly monitor the pulse energy during a measurement. The laser then passes through an air-spaced Rochon prism (Kogakugiken, Japan), and the extraordinary ray is blocked using an iris which allows the ordinary ray to pass. The laser then passes through a broadband UV quarter waveplate (Kogakugiken, Japan), which is held within a motorized rotation mount. Finally, to calibrate the reflected beam energy versus the energy of the beam used to irradiate the ions, a second pyroelectric energy meter (Ophir PE10) can be moved into the beam to measure the pulse energy following the polarization optics and prior to entering the mass spectrometer. The calibration is done prior to every measurement, and a typical example is shown in Fig. S8. The beam passes through a fused silica window into the pass spectrometer, and through 1.7 mm holes in the ring electrode of the ion trap. The beam is reflected by two 45° angle mirrors, and exits the mass spectrometer via a second fused silica window to avoid back scatter of photons within the trap.

The polarization optics and the two irises are connected to the same cage system. This cage system is in turn connected to a high load pitch and yaw platform. This allows the entire polarization optical setup to be moved relative to the beam without changing the laser alignment. To align the laser and polarization optics, first the laser is aligned to the ion trap by monitoring electron detachment yields of $[(TGGGGT)_4 \bullet (NH_4^+)_3]^{5-}$. Next, the caged-mounted polarization optics are positioned so that the laser passes through the center of the two irises, to achieve close to normal incidence of the laser through the polarizer and quarter waveplate. This process is iterated until the laser is aligned to the ions, and the polarization optics are aligned to the laser. The next step is to align the fast axes of the polarizer and the quarter waveplate. To do this, we first orient the linear polarizer to maximize the pulse energy in the ordinary ray. Next, we take advantage of a dependence of the pulse energy transmitted by the quarter waveplate on the rotation angle of the quarter waveplate fast axis at 260 nm, which shows a maximum when the fast axes are aligned, and a minimum when at 90°. The rotation angle of the quarter waveplate is changed from -90° to 90° in 15° steps, and the transmitted and reflected pulse energies measured for 30 seconds. The zero offset of the motorized rotation mount is then optimized to give a maximum in the ratio of transmitted to reflected pulse energy at 0°, Fig. S5.

The beam then passes into the mass spectrometer (AmaZon, Bruker Daltonics, Germany) through 1.7 mm holes in the ring electrode. The ions are produced by electrospray ionization of solutions as described above. The ions are guided into the ion trap, accumulated for between 80 and 90 ms and mass selected with an m/z window of 5 Da where they are stored for 40 ms. During the trapping time, the shutter is opened to admit a single laser pulse into the mass spectrometer. The pulse energy is chosen so that only loss of a single electron is observed in the mass spectrum, and so that the electron detachment yield is still linear with respect to pulse energy, see Fig. S3.

Polarimetry

The polarization state of the laser in the ion trap is measured by polarimetry, using a system of polarizers that duplicates the experimental configuration as closely as possible, Fig. S6. An additional prism was added just after the mechanical shutter to guide the laser through the polarimeter. The polarimeter is comprised of four optical elements. The first linear polarizer and achromatic broadband quarter waveplate (Kogakugiken, Japan, which performance is being characterized herein) are the same as used for CDMS experiments. Next, a second achromatic broadband quarter waveplate (B. Halle, Germany) is placed in a second motorized rotation mount. Finally, an alpha-BBO Glan-laser polarizer is placed, with a rotation angle of 0° that remains fixed throughout all polarimetry measurements. A pyroelectric energy meter (Ophir PE9-C) is placed after the polarimetry setup to measure the pulse energy. Between the two quarter waveplates, a fused silica window identical to that in the vacuum manifold of the mass spectrometer is used. The separation of the first polarizer, quarter waveplate and fused silica window are as close to real experimental conditions as possible.

The fast axis of the first air-spaced Rochon prism (Kogakugiken, Japan) is used to define 0° for the other waveplates. First, the fast axis of the alpha-BBO Glan-laser polarizer was aligned. This was performed by finding the rotation angle of the alpha-BBO Glan-laser polarizer which maximized the pulse energy, without the quarter waveplates present. The angle of the linear polarizers is then fixed throughout. Next, we aligned the quarter waveplates individually. The first quarter waveplate was added to the system. The fast axis angle was then rotated from -90° to 90° and the pulse energy monitored, and the maximum denotes a fast axis angle of 0°. The second quarter waveplate was then added, and the same procedure was used. This ensured that all the optical elements where aligned to the fast axis of the linear polarizer.

In order to measure the polarization state of the laser, the rotation angle ϕ of the first quarter waveplate is fixed to a specific value. The rotation angle θ of the second quarter waveplate is changed between -90° and 90° in 15° steps, and the intensity of the transmitted light averaged for 30 seconds. The intensity of the laser pulse after traversing the polarimeter is given by *(32)*.

$$I(\theta) = \frac{1}{2}(A + B\sin 2\theta + C\cos 4\theta + D\sin 4\theta) \qquad (1)$$

Where the coefficients *A*, *B, C* and *D* are related to the Stoke's parameters S_0, S_1, S_2 and S_3 by:

$$A = S_0 + \frac{S_1}{2}, B = S_3, C = \frac{S_1}{2}, D = \frac{S_2}{2} \qquad (2)$$

The polarization state of the laser was measured at 295 nm, 260 nm and 240 nm. These wavelengths were chosen because they are diagnostic for DNA G-quadruplex topologies. The results are shown in Fig. S7 for $\phi = \pm 45°$ of the first quarter waveplate. Each curve has a dominant $\sin 2\theta$ component, which indicates highly pure circularly polarized radiation. The S_3 parameters extracted from the fit of this data are shown in Table S1. The S_3 parameter is greater than 0.95 for all wavelengths for $\phi = \pm 45°$, indicating that the polarization is at least 95% circularly polarized, which demonstrates excellent performance for our achromatic broadband quarter waveplate. The sign of the S_3 parameter identifies the helicity of the circular polarization. An angle of 45° gives left-handed circular polarized light, and -45° gives right-handed circular polarized light.

Finally, the stability and accuracy of the motorized rotation mount was tested. This is critical for circular dichroism measurements, where the quarter waveplate will be switched between $\phi = +45°$ and $\phi = -45°$ frequently. Polarimetry measurements were made by switching between 45° and -45° and repeating five times, Fig. S7. It can be seen that there is essentially no differences between the different repeated measurements. We can conclude that the motorized rotation mount is able to reproducibly reach the same rotation angle.

Circular dichroism mass spectrometry

The electrospray source of the mass spectrometer and the ion transmission conditions were tuned to avoid harsh collisions yet ensure efficient ion transfer: the syringe flow rate was 3 µL/min; the electrospray voltage was 3000 V, -200 V were applied on the HV endplate; the source conditions were: nebulizer at 14 psi, drying gas at 5 L/min and 220 °C; ehe capillary exit voltage was set to -140 V with the funnel entrance at -100 V; the funnel 1 exit voltage was -35 V. The parent ion was mass-selected with a window of 5 m/z except for 23TAG, for which a window of 20 m/z was used to co-isolate the 1-K^+ and the 2-K^+ complexes. The accumulation time was varied depending on the species, and adjusted to avoid overfilling the trap. The trapping time was 40 ms in all cases, and the mass spectrometer was synchronized with the laser to always allow a single laser pulse during that time window. The mass scan was performed in 'Ultrascan' mode (fastest scan, lowest mass resolution). Although we lose the isotopic resolution (with the advantage that each peak is *de facto* smoothed), we can still distinguish the (NH_4^+ or K^+) adducts distribution and this was sufficient for our purpose. For a given total acquisition time, we found that performing more mass scans per second (here, 3.3 Hz) in the 'Ultrascan' mode gave better statistics on the intensity ratios.

Circular dichroism measurements in solution are performed by measuring the absorption using alternating pulses of left- and right-handed circularly polarized light. For gas phase measurements, we use action spectroscopy, and monitor the relative electron detachment efficiency, defined as:

$$Y_{ePD} = \frac{I_{ePD}}{I_{total}} / (\lambda * E) \qquad (3)$$

where I_{ePD} is the area under the peak in the mass spectrum due to electron detachment, I_{total} is the total area of the precursor ion and the ePD product, and λ is the wavelength and E is the pulse energy. For DNA structures analyzed separately, given the high signal-to-noise ratio the I_{total} was

conveniently approximated by area under the total mass spectrum. For the analysis of the mixture of two stoichiometries in the case of 23TAG, the precursor and product ions were integrated individually.

First, we must find the optimal conditions to reproducibly measure the relative electron detachment efficiency. Two competing factors must be considered. One the one hand, it is desirable to change the polarization as often as possible, in order to minimize changes in the overlap of the ion cloud and laser, or changes in the pulse energy or beam profile. On the other hand, it is necessary to acquire mass spectra long enough to obtain an accurate measurement of the relative electron detachment efficiency. We found that a 90 second acquisition time was optimal to balance these two considerations.

The methodology used to perform gas-phase circular dichroism measurements is as follows. The wavelength and polarization state of the laser is fixed, and the trapped ions are irradiated with a single laser pulse. The mass spectrum is averaged for 90 seconds (except all the experiments on the strand 23TAG: 180 s). As noted above, the ratio of transmitted to reflected pulse energy is sensitive to the rotation angle of the quarter waveplate. Therefore, the reflected pulse energy cannot be used alone for normalization. Thus, at each wavelength a calibration of transmitted and reflected pulse energy is performed prior to recording mass spectra. The rotation angle of the quarter waveplate is fixed to 45°, and the reflected and transmitted pulse energy averaged for a period of 30 seconds for a series of neutral density filters between 0 and 1 optical density in 0.1 steps. This process is then repeated with the quarter waveplate rotation angle fixed to 315°. Fig. S8 shows the reflected vs transmitted pulse energy for 45° and -45°, which have a linear correlation. The data is fitted with a linear function of the form $y = ax + b$, which is used to convert the reflected pulse energy recorded during a circular dichroism measurement to the transmitted pulse energy, which is then used for normalization.
Next, the quarter waveplate rotation angle is fixed to 45°, the trapped ions are irradiated and the mass spectrum averaged for 90 seconds. The rotation angle is then changed to -45° and the mass spectrum averaged for 90 seconds. This process is repeated 10 times, giving a total irradiation time of 30 minutes (60 minutes for the experiments on 23TAG, Fig. 3). This process is then repeated for each wavelength used.

In order to extract the circular dichroism value, the relative electron detachment efficiency is determined for each mass spectrum acquired above, giving 10 values for RCP and LCP using equation 3. The average value of the relative detachment efficiency for RCP and LCP is determined.

$$\overline{Y_{ePD}^{RCP}} = \frac{\sum_n Y_{ePD}^{RCP}}{n} \qquad (4)$$

$$\overline{Y_{ePD}^{LCP}} = \frac{\sum_n Y_{ePD}^{LCP}}{n} \qquad (5)$$

Circular dichroism is defined as the difference in absorption of left- and right-handed circular polarized photons. Here, we can make the assumption that the relative electron detachment

efficiency is directly correlated to the absorption cross-section. Following the convention for circular dichroism measurements, we define the asymmetry factor g_{ePD} as:

$$g_{ePD} = \frac{\Delta ePD}{\overline{ePD}} = 2 * \left(\frac{\overline{Y_{ePD}^{LCP}} - \overline{Y_{ePD}^{RCP}}}{\overline{Y_{ePD}^{LCP}} + \overline{Y_{ePD}^{RCP}}} \right) \qquad (6)$$

This gives a unitless value for the circular dichroism, which can be directly compared to solution phase measurements.

$$CD = g_{sol} = \frac{\Delta A}{\bar{A}} = \frac{\Delta \epsilon}{\bar{\epsilon}} \qquad (7)$$

Where A is the absorbance and ϵ is it extinction coefficient.

In order to determine the reproducibility of circular dichroism mass spectrometry measurements, two different methodologies were used. Firstly, for each species the circular dichroism measurements are repeated 3 times for at least wavelength. The standard error in the repeated measurements is then determined and reported.

Solution Phase circular dichroism

All solution phase measurements were performed on a JASCO 1500 circular dichroism spectrometer. The samples for the circular dichroism measurements were prepared in an identical manner as those used in mass spectrometry, as described above. Spectra were recorded between 350 and 220 nm, and blank subtractions performed. For data analysis, the circular dichroism in mdeg was first converted to ΔA using the conversion factor:

$$CD(\Delta A) = \frac{CD(mdeg)}{32980} \qquad (8)$$

The asymmetry factor as then calculated as

$$g_{sol} = \frac{\Delta A}{A} \qquad (9)$$

The absorbances A were measured on a SAFAS UV mc² double-beam spectrophotometer (Montecarlo, Monaco) furnished with a Peltier temperature controller.

Ion Mobility Mass Spectrometry

The experiments were carried out on an Agilent 6560 IMS-Q-TOF (Agilent Technologies, Santa Clara, CA), with its drift tube ion mobility cell operated in helium. The instrument tuning parameters are the same as the "compromised" tuning parameters described and discussed elsewhere (penultimate column of Tables 1 and 2 in (*33*)). The helium pressure in the drift tube was 3.89 ± 0.01 Torr, and the pressure in the trapping funnel is 3.63 ± 0.01 Torr. The pressure differential between the drift tube and the trapping funnel ensures only helium is present in the drift tube. Injection was in negative ion mode, using the standard electrospray source and a syringe pump at 4 µL/min. The acquisition software version was B.07.00 build 7.00.7008. The

arrival time distributions were extracted from the entire isotopic distribution of each adduct, using IM-MS browser.

Step-field experiments (five drift tube voltages for each samples) were performed to determine the CCS. The arrival time distributions (ATDs) for each charge state of the complexes were fitted with one gaussian peak using OriginPro 2016, to determine the arrival time t_A of the center of the peak. The arrival time t_A is related to ΔV (voltage difference between the entrance and the exit of the drift tube region) by:

$$t_A = \frac{L^2}{K_0}\frac{T_0 p}{p_0 T} \cdot \left(\frac{1}{\Delta V}\right) + t_0 \quad (10)$$

t_0 is the time spent outside the drift tube region and before detection. A graph of t_A vs. $1/\Delta V$ provides K_0 from the slope and t_0 as the intercept. The drift tube length is L = 78.1 cm, the temperature is measured accurately by a thermocouple (here, T = 297 ± 1 K), and the pressure is measured by a capacitance gauge (p = 3.89 ± 0.01 Torr). The CCS is then determined using Equation (11):

$$CCS = \frac{3ze}{16N_0} \cdot \sqrt{\frac{2\pi}{\mu k_B T}} \cdot \frac{1}{K_0} \quad (11)$$

The reconstruction of the experimental CCS distributions from the arrival time distributions at the lowest voltage is then performed using Equation (12), where the factor a is determined from the t_A of the peak center at the lowest voltage and the CCS calculated from the regression described above, from the peak centers.

$$CCS = a \cdot \frac{z}{\sqrt{\mu}} \times t_A \quad (12)$$

Generation of gas-phase structures and calculation of theoretical collision cross sections

The gas-phase modeling was started from the published structure (PDB code: 1S45 for TG4T, 5YEY for the antiparallel G-quadruplex, 4U5M for the Z-G4 and ref (*20*) for GAgG11). Phosphate groups (arbitrarily chosen) where neutralized by protons to attain a total charge state of 5- or 6-. We optimized the structure at the semi-empirical level with PM7 (*34*) parameterization, using Gaussian 16 rev. B.01 (*35*). Then, atom Centered Density Matrix Propagation molecular dynamics (ADMP, 1000 fs, 296 K) at the semi-empirical level (PM7) was performed. The theoretical CCS values were calculated for a structure every 10 fs, using the trajectory model (Mobcal (*36*), original parameters for helium, N and O parameterized as C, P and K parameterized as Si). The GAgG11 structure is calculated as described in ref (*20*).

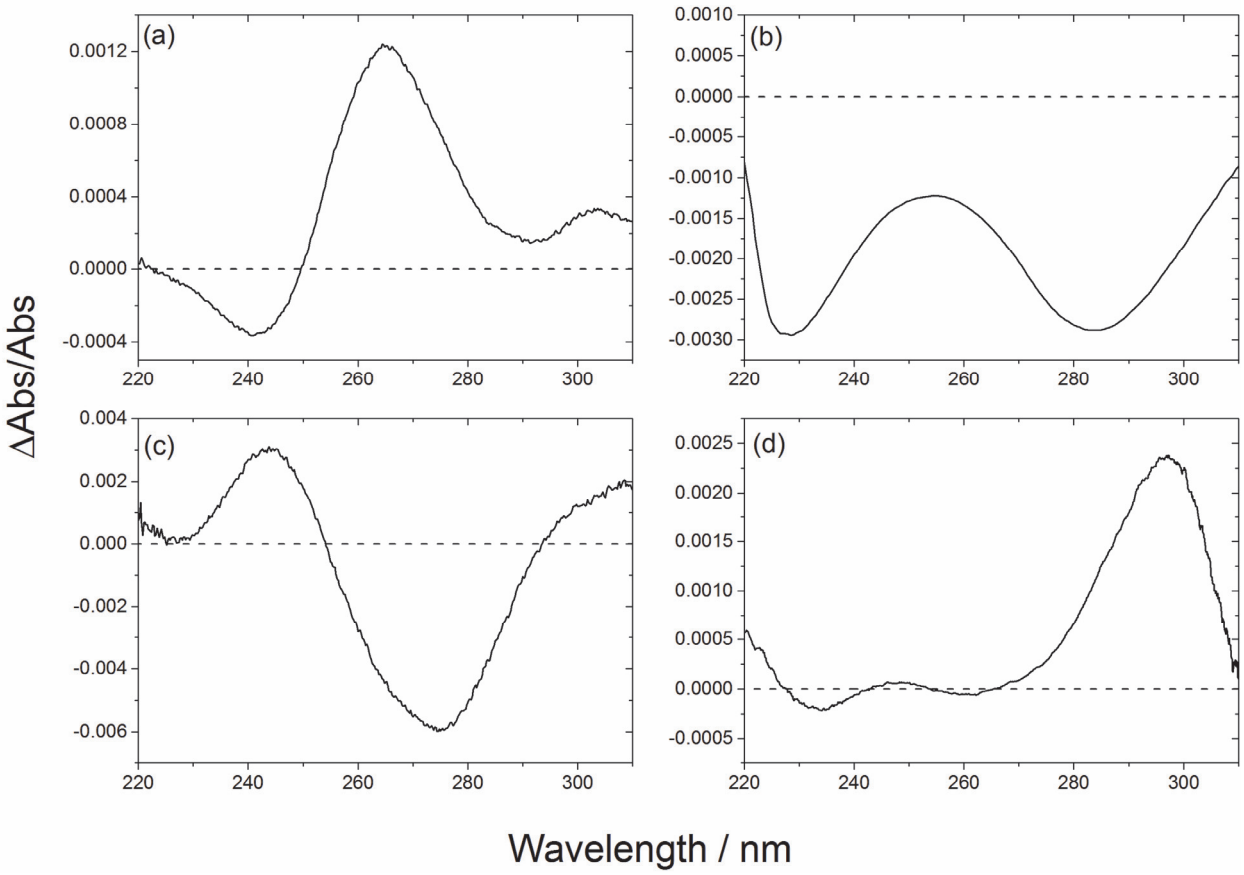

Fig. S1. Solution phase electronic circular dichroism spectra (all D-sugars).

(a) TG4T (5 μM tetramolecular G-quadruplex, 100 mM ammonium acetate), (b) GAgG (5 μM duplex, 60 μM $AgNO_3$, 20 mM ammonium acetate), (c) ZG4 (5 μM $dT(GGT)_4TG(TGG)_3TGTT$, 100 mM ammonium acetate) and (d) 5YEY (5 μM $d(GGGTTA)_2GGGTTTGGG$, 1 mM KCl, 100 mM trimethylammonium acetate).

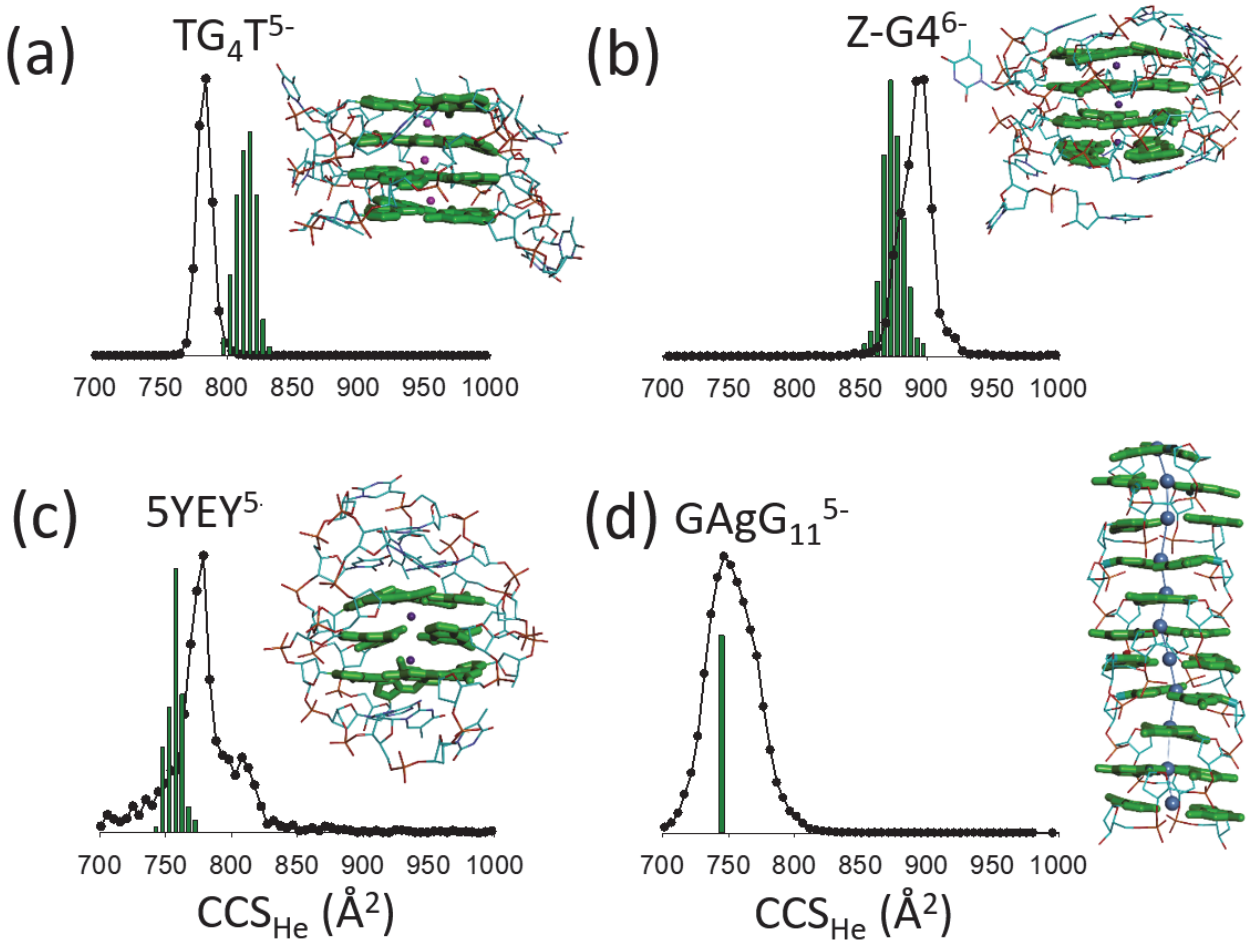

Fig. S2. Gas-phase ion mobility spectrometry and calculated collision cross sections.

Black dots: Experimental helium collision cross section distributions reconstructed for (a) $[(dTGGGGT)_4 \bullet (NH_4^+)_3]^{5-}$, (b) $[d(GGGTTA)_2GGGTTTGGG \bullet (K^+)_2]^{5-}$, (c) $[dT(GGT)_4TG(TGG)_3TGTT \bullet (NH_4^+)_3]^{6-}$ and (d) $[(dG_{11})_2 \bullet (Ag^+)_{11}]^{5-}$. Green bars: calculated helium collision cross sections for a collection of gas-phase structures generated by PM7 optimization followed by PM7 BOMD, except for GAgG (panel d) for which the structure was generated as described in (*20*), and PM7 BOMD was not feasible due to inappropriate parameterization of silver.

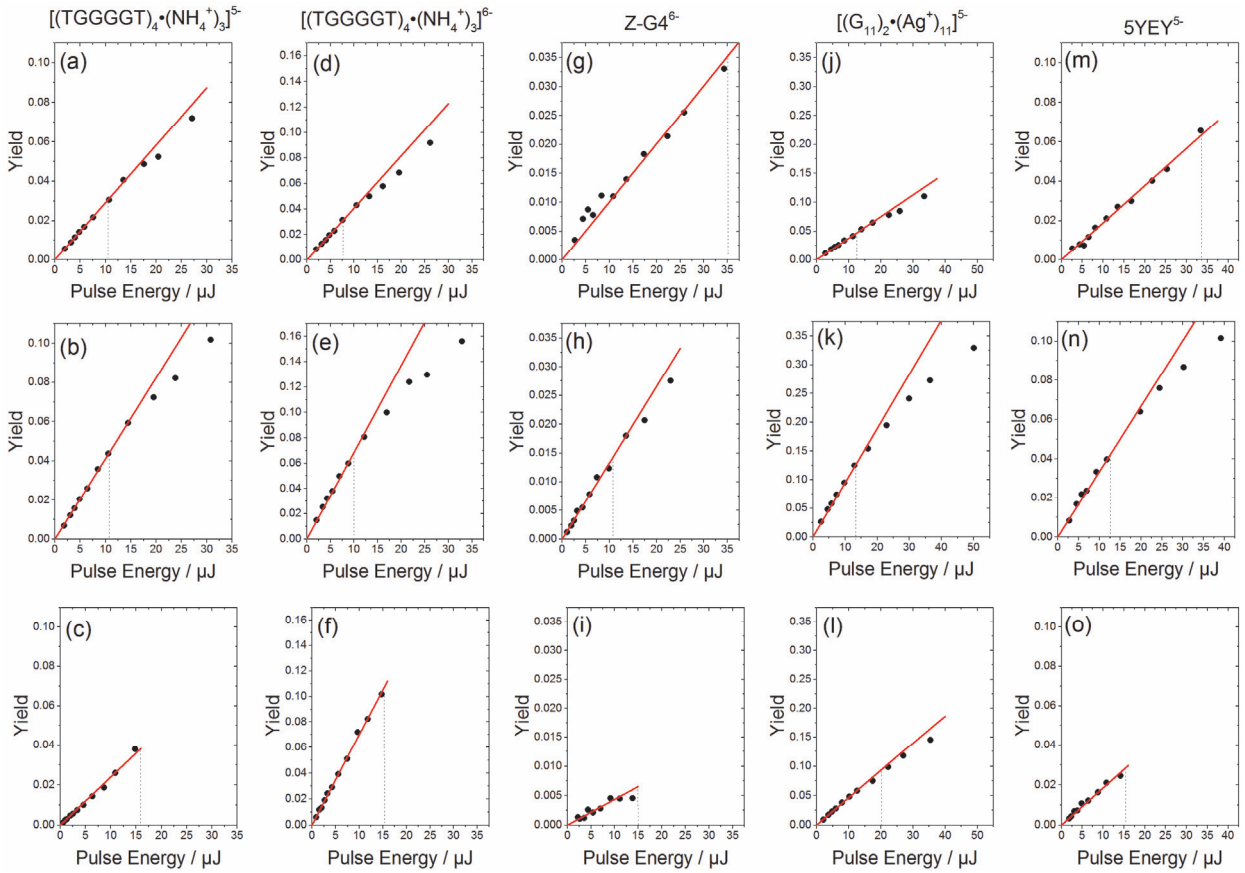

Fig. S3. Linearity of the electron photodetachment process.

Electro n detachment yield (I_{ePD}/I_{total}) as a function of the laser pulse energy of $TG4T^{5-}$ ions at (a) 240 nm, (b) 260 nm and (c) 280 nm$TG4T^{6-}$ ions at (d) 240 nm, (e) 260 nm and (f) 280 nm. $ZG4^{6-}$ ions at (g) 240 nm, (h) 260 nm and (i) 280 nm. $[(G_{11})_2\bullet(Ag^{+})_{11}]^{5-}$ ions at (j) 240 nm, (k) 260 nm and (l) 280 nm. $5YEY^{5-}$ ions at (m) 240 nm, (n) 260 nm and (o) 280 nm. The red line represents a linear fit to the data passing through the origin.

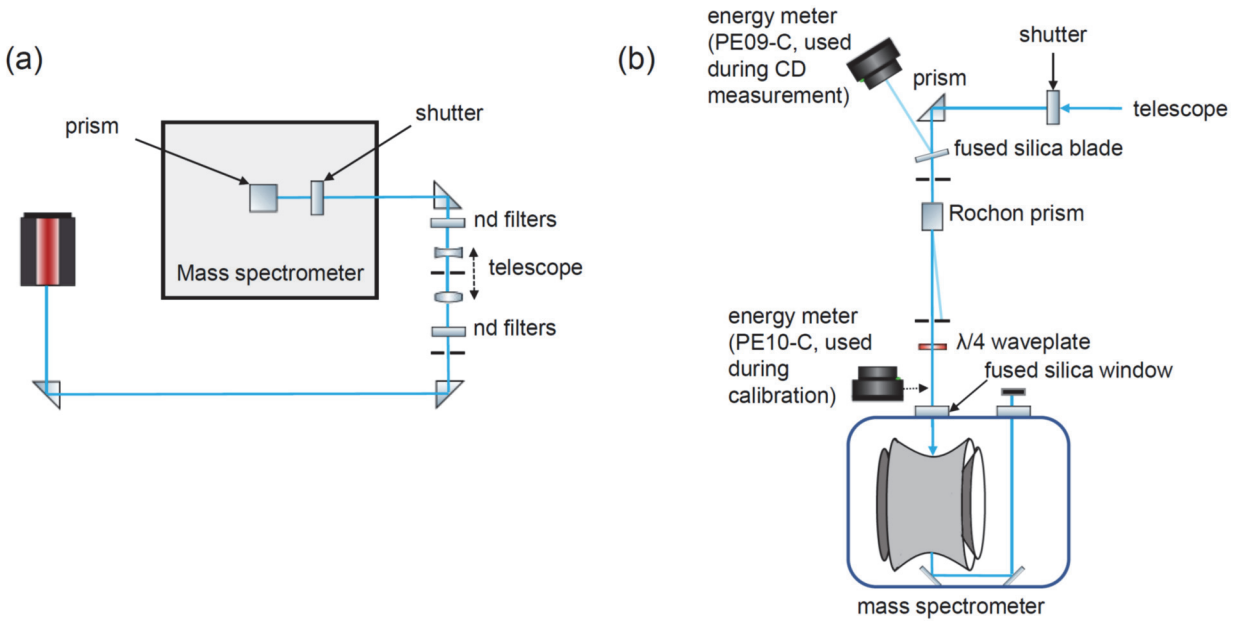

Fig. S4. Experimental setup used for circular dichroism mass spectrometry.

(a) Top view showing the laser, the neutral density filters used to control pulse energy and the telescope used to collimate the beam. (b) Side view of the polarization optics. The beam passes through a shutter, is reflected through 90° by a prism and through a fused silica blade. This reflects a small portion of the beam to a power meter (PE09-C) which is used to record the pulse energy during mass spectrum acquisitions. The beam then passes through the polarization optics. A second pulse energy meter (PE10-C) can be inserted into the beam just before the mass spectrometer, and is used to convert reflected pulse energies to transmitted pulse energy for normalization. The beam then passes through a fused silica window, through a Paul trap, is reflected by two 45° mirrors and exits the mass spectrometer through a second fused silica window, where it is blocked.

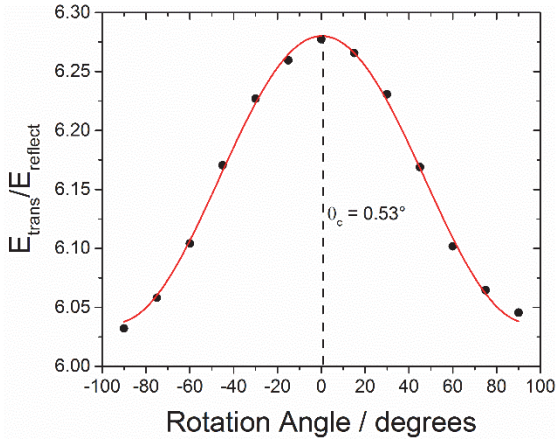

Fig. S5. Verification of the quarter wave plate.

Ratio of transmitted to reflected pulse energy as a function of the fast axis angle of the quarter waveplate (black squares) at 260 nm. The red line is a fit to a cosine function $y = y_0 + A\cos\left[\frac{(x-x_c)\pi}{p}\right]$. The value x_c gives the offset between the fast axis of the quarter waveplate and the linear polarizer.

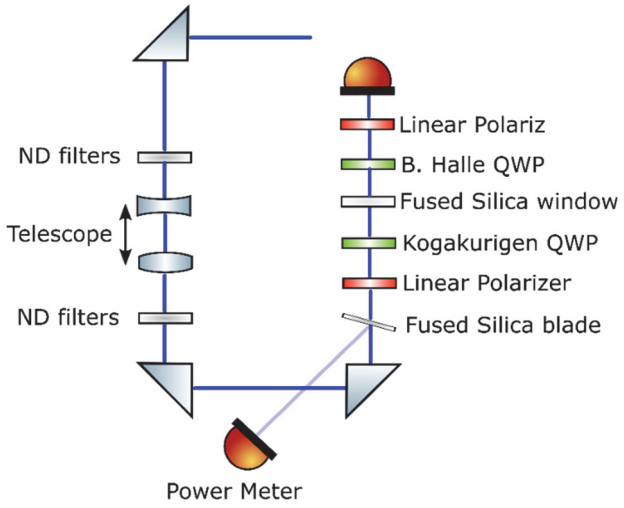

Fig. S6. Polarimetry setup for confirming the polarization state of laser pulses.

An additional prism is added after the shutter in Fig. S1. The fused silica blade, linear polarizer and first quarter waveplate are in an identical configuration as used in CDMS experiments. The fused silica window is identical to the one in the vacuum manifold to allow light to couple to the ion trap. The second quarter waveplate and linear polarizer are used to measure the polarization after the fused silica window.

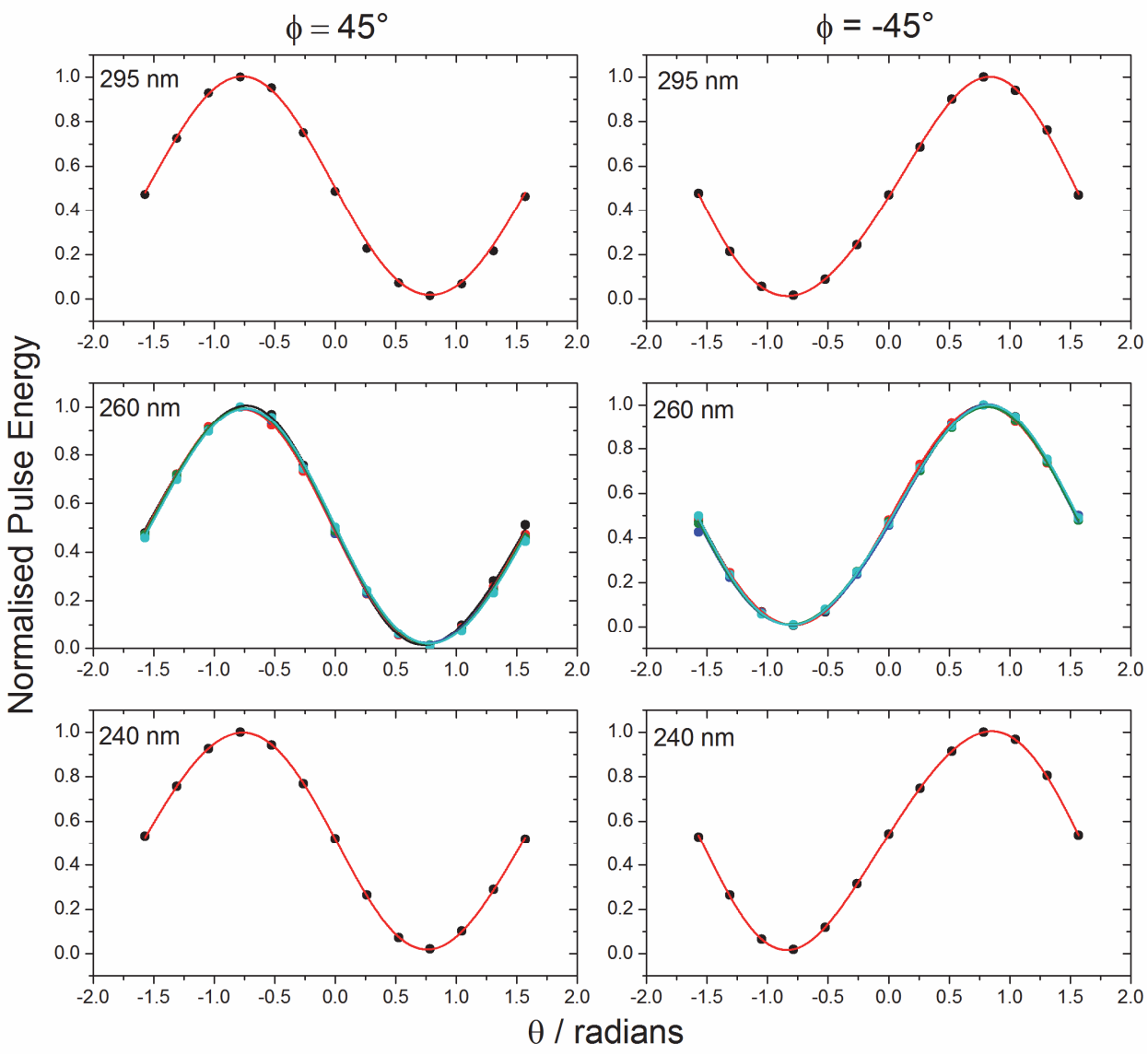

Fig. S7. Polarimetry results.

Normalized pulse energy (circles) as a function of the second quarter waveplate angle θ for $\phi = \pm 45°$ of the first quarter waveplate at 295 nm (top), 260 nm (middle) and 240 nm (bottom). The red curve shows the fit to the function in equation 1. For 260 nm, 5 measurements were made to show the reproducibility of the polarization and that there was no change when repeatedly cycling form 45° to -45° and back.

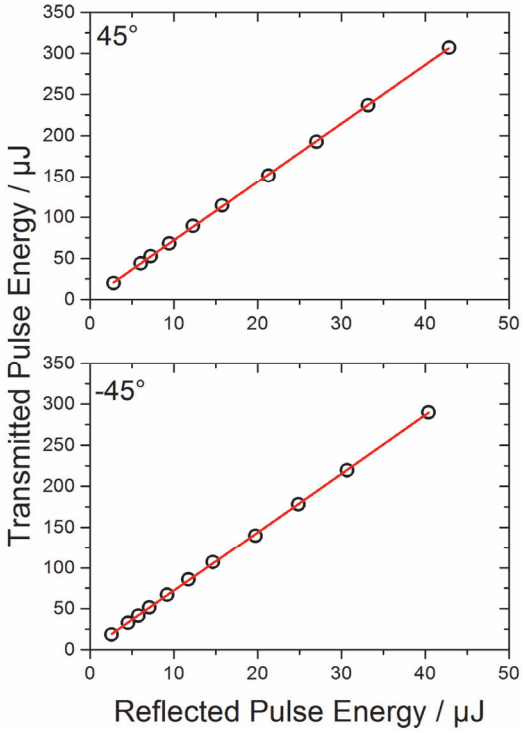

Fig. S8. Calibration of the transmitted vs. reflected laser pulse energy.

Transmitted versus reflected pulse energy at 260 nm for 45° (top) and -45° (bottom) rotation angle of the quarter waveplate, using neutral density filters to give optical densities between 0 and 1.0 (circles). The red line is a linear fit ($y = ax + b$) of the data, which is used to convert the reflected pulse energy averaged during measurement of a mass spectrum to the transmitted pulse energy that can be used for normalization in equation 3.

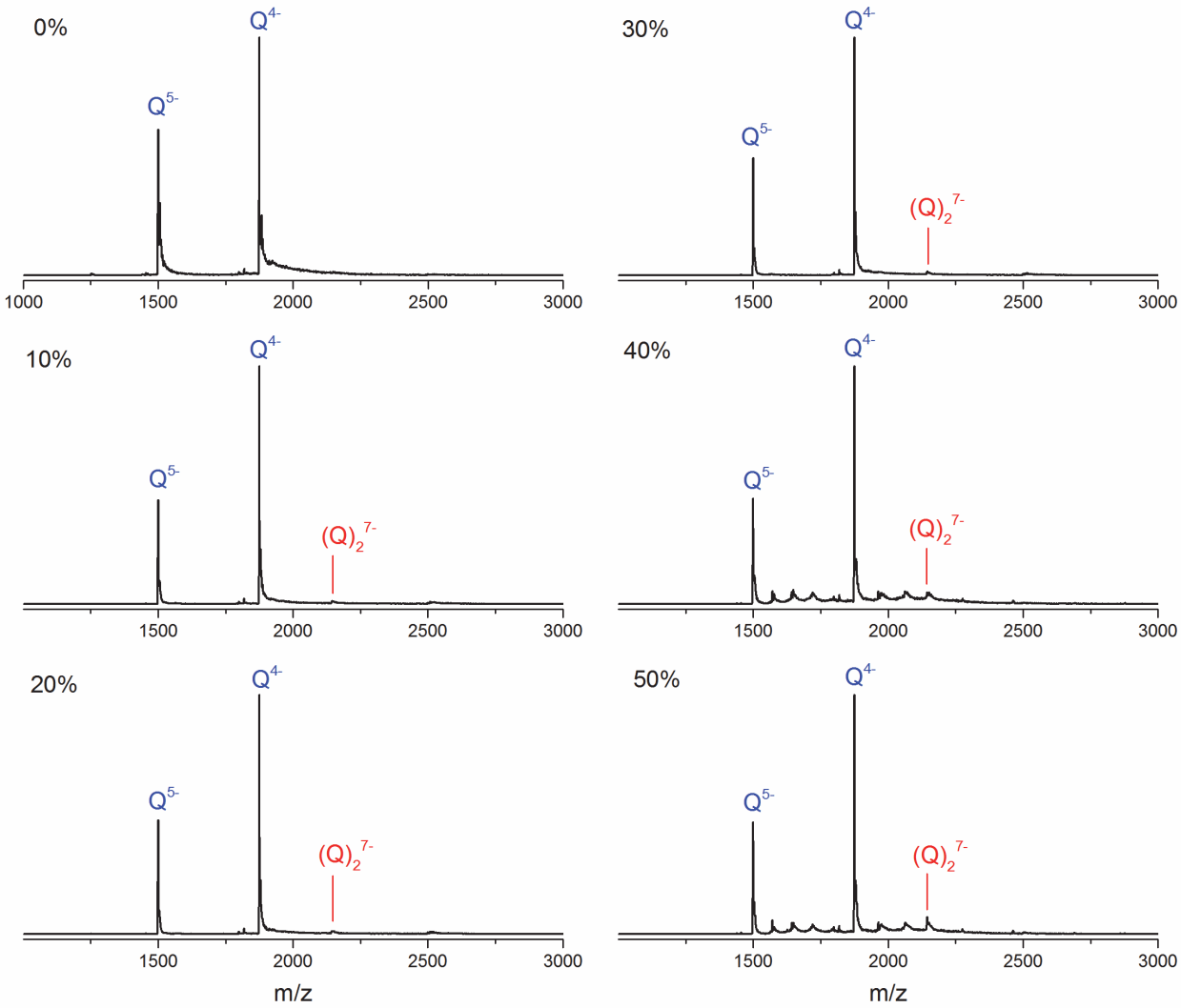

Fig. S9. Addition of up to 50% isopropanol does not cause aggregation of TG4T.

Mass spectra of TGGGGT in 100mM ammonium acetate at different percentages v/v of isopropanol. Q denotes the intact quadruplex structures $[(TGGGGT)_4 \bullet (NH_4^+)_3]$, and S denotes the single strand. There is no significant change in the mass spectra as a function of the isopropanol concentration. Above 40%, some adducts appear, but there is no evidence for the formation of any higher order oligomers, or for significant disruption of the quadruplexes.

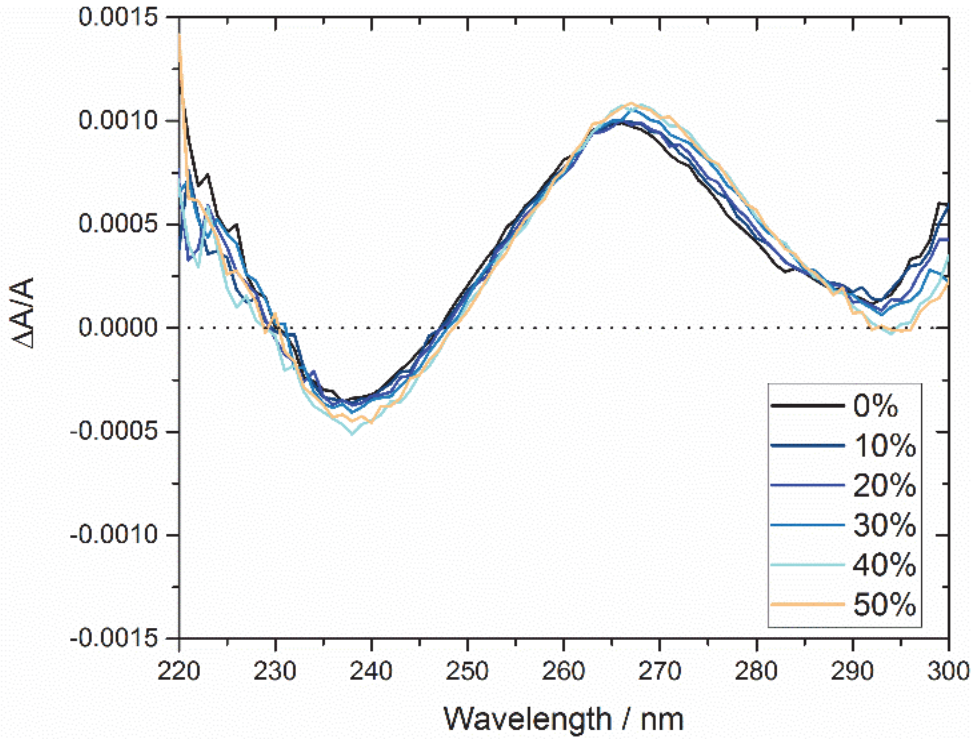

Fig. S10. In solution, the solvent polarity does not affect the CD spectrum of TG4T.

Circular dichroism spectra for 5μM *D*-[(TGGGGT)$_4$•(NH_4^+)$_3$] in 100 mM ammonium acetate for different volume percentages of isopropanol.

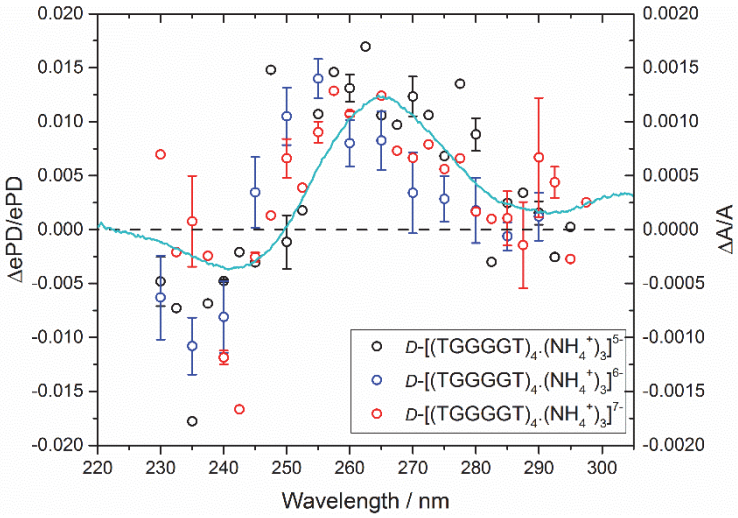

Fig. S11. The charge state does not affect the magnitude of the gas-phase CD effect.

Gas phase circular dichroism (circles) for D-[(TGGGGT)$_4$•(NH_4^+)$_3$] in the 5- (black), 6- (red) and 7- (blue) charge states. Charge states 6- and 7- were obtained by lowering the ammonium acetate concentration to 20 mM. Errors bars represent the standard error in 3 repeated measurements. The cyan curve shows the solution phase circular dichroism of D-[(TGGGGT)$_4$•(NH_4^+)$_3$] in 100 mM ammonium acetate.

Table S1. S_3 parameters for the data shown in Fig. S6.

The values in parentheses represent the error in the fitting procedure for 240 nm and 295 nm. For 260 nm, the values are the standard error in the 5 repeated measurements.

	45° (LCP)	**-45° (RCP)**
240 nm	-0.963(6)	0.962(5)
260 nm	-0.960(2)	0.980(1)
295 nm	-0.965(22)	0.969(9)

Table S2. Details of the replicates for main text Figure 3B.

Wavelength (nm)	Number of replicates
235	3
240	7
245	9
250	13
255	15
260	21
265	9
270	7
275	8
280	11
285	9
290	14

References

1. F. Arago, *Mém. Class Sci. Math. Phys. Inst. Impérial France* **1**, 93-164 (1811).
2. S. W. Smith, *Toxicol. Sci.* **110**, 4-30 (2009).
3. J. D. Watson, F. H. C. Crick, *Nature* **171**, 737-738 (1953).
4. R. E. Franklin, R. G. Gosling, *Nature* **171**, 740-741 (1953).
5. I. Liko, T. M. Allison, J. T. Hopper, C. V. Robinson, *Curr. Opin. Struct. Biol.* **40**, 136-144 (2016).
6. P. Lossl, M. van de Waterbeemd, A. J. Heck, *EMBO J.* **35**, 2634-2657 (2016).
7. F. W. McLafferty, *Science* **214**, 280-287 (1981).
8. D. E. Clemmer, M. F. Jarrold, *J. Mass Spectrom.* **32**, 577-592 (1997).
9. E. Garand *et al.*, *Science* **335**, 694-698 (2012).
10. J. Seo *et al.*, *Nat. Chem.* **9**, 39-44 (2017).
11. M. Z. Kamrath, T. R. Rizzo, *Acc. Chem. Res.* **51**, 1487-1495 (2018).
12. H. Awad, A. El-Aneed, *Mass Spectrom. Rev.* **32**, 466-483 (2013).
13. W. A. Tao, F. C. Gozzo, R. G. Cooks, *Anal. Chem.* **73**, 1692-1698 (2001).
14. J. Kypr, I. Kejnovska, D. Renciuk, M. Vorlickova, *Nucleic Acids Res.* **37**, 1713-1725 (2009).
15. A. J. Miles, B. A. Wallace, *Chem. Soc. Rev.* **35**, 39-51 (2006).
16. R. Li, R. Sullivan, W. Al-Basheer, R. M. Pagni, R. N. Compton, *J. Chem. Phys.* **125**, 144304 (2006).
17. U. Boesl von Grafenstein, A. Bornschlegl, *ChemPhysChem* **7**, 2085-2087 (2006).
18. A. Hong *et al.*, *Angew. Chem. Int. Ed.* **53**, 7805-7808 (2014).
19. W. J. Chung *et al.*, *Proc. Natl. Acad. Sci. USA* **112**, 2729-2733 (2015).
20. C. Liu *et al.*, *Chem. Sci.* **10**, 218-226 (2018).
21. S. M. Swasey, F. Rosu, S. M. Copp, V. Gabelica, E. G. Gwinn, *J. Phys. Chem. Lett.* **9**, 6605-6610 (2018).
22. V. Gabelica *et al.*, *J. Am. Chem. Soc.* **130**, 1810-1811 (2008).
23. V. Gabelica *et al.*, *Anal. Chem.* **78**, 6564-6572 (2006).
24. F. Rosu *et al.*, *J. Phys. Chem. A* **116**, 5383-5391 (2012).
25. S. Daly, M. Porrini, F. Rosu, V. Gabelica, *Faraday Discuss.* **217**, 361-382 (2019).
26. P. Horsch, G. Urbasch, K. M. Weitzel, D. Kroner, *Phys. Chem. Chem. Phys.* **13**, 2378-2386 (2011).
27. H. G. Breunig *et al.*, *ChemPhysChem* **10**, 1199-1202 (2009).
28. J. Lepelmeier, K. Titze, A. Kartouzian, U. Boesl, U. Heiz, *ChemPhysChem* **17**, 4052-4058 (2016).
29. L. Nahon, G. A. Garcia, C. J. Harding, E. Mikajlo, I. Powis, *J. Chem. Phys.* **125**, 114309 (2006).
30. M. H. Janssen, I. Powis, *Phys. Chem. Chem. Phys.* **16**, 856-871 (2014).
31. A. R. de Souza, V. F. Ximenes, N. H. Morgon, in *Stereochemistry and Global Connectivity: The Legacy of Ernest L. Eliel Volume 2*. (2017), pp. 91-101.
32. V. Gabelica *et al.*, *J. Am. Chem. Soc.* **129**, 4706-4713 (2007).
33. A. T. Phan, *FEBS J.* **277**, 1107-1117 (2010).
34. A. Marchand, V. Gabelica, *Nucleic Acids Res.* **44**, 10999-11012 (2016).
35. A. I. Karsisiotis *et al.*, *Angew. Chem. Int. Ed.* **50**, 10645-10648 (2011).
36. S. Daly, F. Rosu, V. Gabelica, *Zenodo,* DOI: 10.5281/zenodo.3758200 (2020).

37. B. Schaefer, E. Collett, R. Smyth, D. Barrett, B. Fraher, *Am. J. Phys.* **75**, 163-168 (2007).
38. V. Gabelica, S. Livet, F. Rosu, *J. Am. Soc. Mass Spectrom.* **29**, 2189-2198 (2018).
39. J. J. Stewart, *J. Mol. Model.* **19**, 1-32 (2013).
40. M. J. Frisch *et al.*, *Gaussian 16 Rev. B.01*. (Wallingford, CT, 2016).
41. M. F. Mesleh, J. M. Hunter, A. A. Shvartsburg, G. C. Schatz, M. F. Jarrold, *J. Phys. Chem.* **100**, 16082-16086 (1996).